Journal of Magnetics 22(4), 579-589 (2017)
ISSN (Print) 1226-1750
ISSN (Online) 2233-6656
https://doi.org/10.4283/JMAG.2017.22.4.579

Normal Force and Vibration Analysis of Linear Permanent-Magnet Vernier Machine

Yanxin Mao, Guohai Liu*, and Huawei Zhou

School of Electrical and Information Engineering, Jiangsu University, Zhenjiang 212013, China

(Received 11 February 2017, Received in final form 14 November 2017, Accepted 20 November 2017)

This paper presents an analytical method for calculating the magnetic field in a new linear permanent-magnet vernier (LPMV) machine, thus predicting the electromagnetic vibration. The main vibration source is the normal force between the mover and the stator of the LPMV machine. Firstly, the air-gap flux density is calculated and analyzed using the rotor permeance to modulate the magneto-motive force, and is verified by the finite element (FE) results. Then, the harmonics of the normal force density is calculated, the normal force and thrust force are analyzed. Secondly, the natural vibration modes and the transient displacement of the mover are predicted by FE method, and the relationship between the normal force density and the vibration is determined. Finally, experimental results are given for verification. This study is instructive for the design of a high-precision and low-vibration LPMV machine.

Keywords : magneto-motive force, normal force density, vibration analysis, linear permanent-magnet machine, vernier

1. Introduction

Permanent-magnet (PM) machine has been paid great attention [1]. Especially, the linear machine has been widely used for their high dynamic performance and can be driven directly without the use of any mechanical converter in direct-drive applications [2-6]. Among them, linear PM vernier (LPMV) machine is more suitable for low-speed and high-torque applications, and some machine topologies with improved electromagnetic properties have been proposed [7-9]. Very recently, a new LPMV machine has been proposed [10] and analyzed [11]. This machine has robust structure, high force density, and low cost, which is very suitable for long stroke applications.

However, the vibration and acoustic noise still seriously affect the operational performance of this linear machine drive. For the LPMV machine, the large normal force is produced between the stator and mover cores in addition to the thrust force, resulting in frictional force perturbation, which greatly influences the thrust force fluctuation and the vibration. Especially, when the frequency of the normal force is same as the natural frequency of the machine, resonance will occur. In fact, the vibration amplitude is determined by the magnetic force and the material properties of the machine. Furthermore, based on the operation principle of the LPMV machine, rich harmonics are produced due to the modulation of the magnetic field, thus emerging abundant lower order harmonics of the normal force density, which is very significant for vibration and noise.

In the development of linear PM machines, most of literatures are based on the electromagnetic analysis or the optimal design [12, 13], rather than the vibration and acoustic noise induced by the normal force. So far, only a few studies have been reported on the normal force or the vibration of a PM linear machine. Recently, two symmetrical structures were proposed to suppress the normal force with PM group shifting of the PM linear machine [14]. In [15], some transverse flux linear machines with different utilizations of PMs were investigated. The results showed that more employment of PMs leads to higher flux concentration in the air-gap and provides higher thrust force.

This paper aims to investigate the normal force and vibration characteristics of the LPMV machine. Firstly, the topology and operation principle of the LPMV machine will be briefly introduced. Secondly, the air-gap flux densities on the PM and armature fields will be analyzed

*Corresponding author: Tel: +86-0511-88791245
Fax: +86-0511-88791245, e-mail: ghliu@ujs.edu.cn

by the magneto-motive force (MMF) and the air-gap surface permeance of the stator. Thirdly, the normal force density will be obtained by finite element (FE) method, the normal force, the thrust force, and the fluctuations are analyzed. Then, the main natural vibration modes and the transient vibration of the mover will be predicted, the relationship between the normal force density and the vibration will be determined. Finally, the experimental measurements will be given for verification.

2. LPMV Machine

The cross-section and the prototype of the three-phase LPMV machine are shown in Fig. 1. Both the PMs and the concentrated armature windings are placed in the short mover, and each armature tooth has four split teeth, while the long stator is designed as a simple iron core with salient poles. Each phase winding is composed of two concentrated coils connected in series. In order to focus the PM flux, the machine adopts the special PM arrays, whose magnetization directions are shown by the arrows in Fig. 1(a). The vertically magnetized PM is sandwiched between the two horizontally magnetized PMs to reduce the PM fringing leakage flux, hence improving air-gap flux density. Every big armature tooth has three PM arrays separated by four split teeth.

The operation principle of the LPMV machine is based on the magnetic field modulation. The 2-pole magnetic field produced by the three-phase armature windings on the mover is modulated by the 20 stator teeth. This modulation produces 18-pole magnetic field in the air-gap which interacts with the 18-consequent-pole PM field on the mover to produce a thrust force. Fig. 2 shows the magnetic field at different mover positions, in which phase B is used as an example. When the vertically magnetized PMs in the mover slot align with the stator

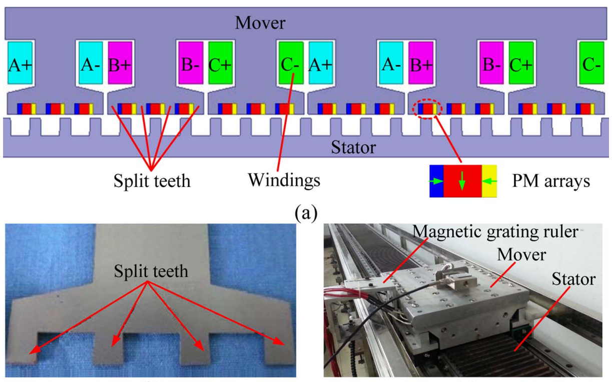

Fig. 1. (Color online) LPMV machine. (a) Topology. (b) Split teeth. (c) Prototype.

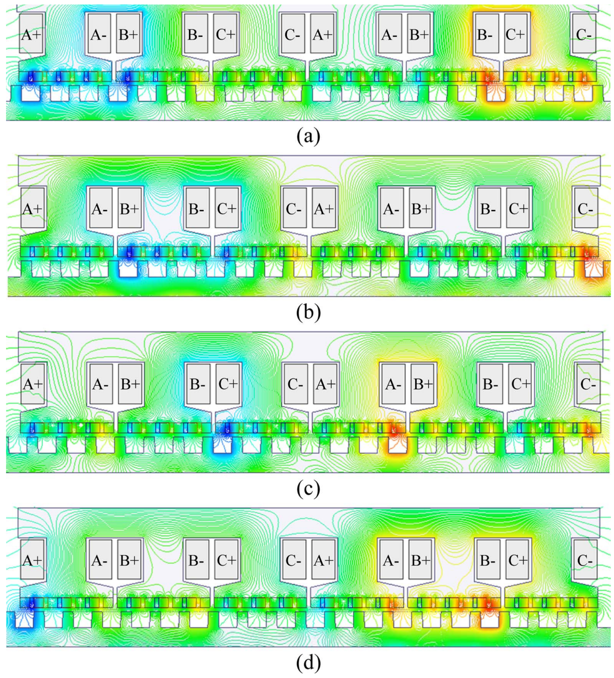

Fig. 2. (Color online) Magnetic field at different positions. (a) 0°. (b) 90°. (c) 180°. (d) 270°.

teeth as shown in Figs. 2(a) and 2(c), the flux linkage of phase B is maximum. In Figs. 2(b) and 2(d), when the horizontally magnetized PMs align with the stator teeth, no flux link phase B at the two positions. It should be noted that both coils of one phase can obtain the maximum or minimum PM flux linkage at the same time. It means that each coil is sufficiently utilized, which results in a high power density in the LPMV machine.

The LPMV machine possesses low cost and mechanical robustness due to the simple long stator core, which is very suitable for long stroke applications. Moreover, since the horizontally magnetized PMs significantly reduce the leakage flux, this machine provides high thrust force density. In addition, the thrust force fluctuation is lower than the cogging force due to appropriate reluctance force [10]. However, this machine still suffers from vibration and acoustic noise originated from the large normal force. This is a significant drawback which will deteriorate the performance of the LPMV machine in high-precision applications. The normal force and the vibration induced by normal force will be investigated in the following discussions.

3. Flux Density Analysis

3.1. Air-Gap Flux Density on No Load

The air-gap PM MMF generated by the PM arrays with consideration of the split teeth is assumed to be a square

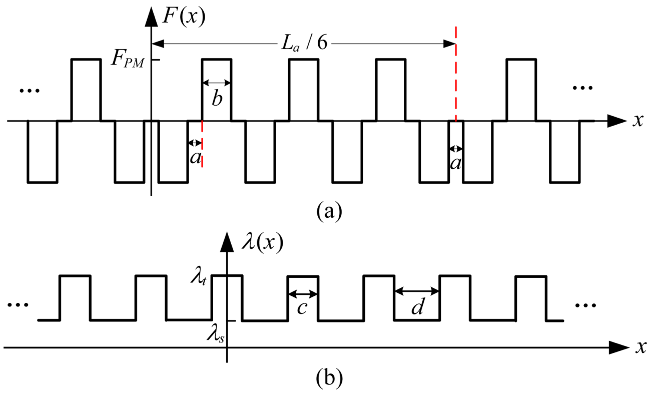

Fig. 3. (Color online) PM MMF and permeance models.

wave with an air-gap circumferential position. Fig. 3(a) shows the air-gap PM MMF in the short mover, and its Fourier series can be derived as

$$F(x) = F_0 + \sum_{n=1}^{\infty} F_n \cos\left(6n\frac{2\pi}{L_a}x\right) \tag{1}$$

where

$$\begin{cases} F_0 = -6F_{PM}\dfrac{b}{L_a} \\ F_n = \dfrac{2F_{PM}}{n\pi}\sin(6n\pi\dfrac{b}{L_a})\displaystyle\sum_{k=1}^{7}(-1)^k\cos\left[6n\pi(2k-1)\dfrac{a+b}{L_a}\right] \end{cases} \tag{2}$$

where x is the air-gap circumferential position, L_a is the effective length of the stator, a and b are the width of the horizontally and vertically magnetized PMs, respectively. According to (1), the $6n$ (n = 1, 2, 3...) harmonic orders of the PM MMF exist because the mover has six armature teeth, as shown in Fig. 1(a), and the spatial harmonics of the PM MMF by (1) are shown in Fig. 4.

The air-gap permeance model with consideration of the stator teeth is shown in Fig. 3(b). Its Fourier series can be expanded as

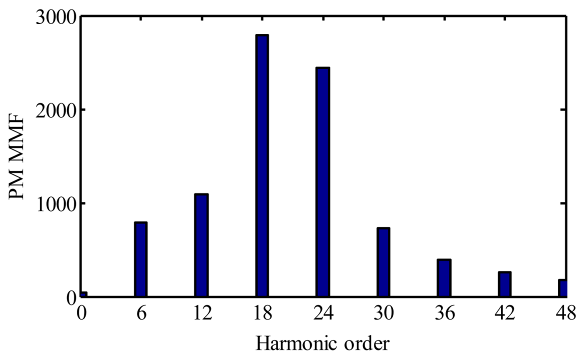

Fig. 4. (Color online) Spatial harmonics of PM MMF by analytical method.

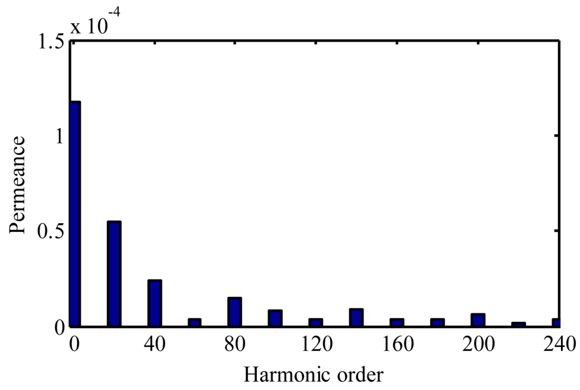

Fig. 5. (Color online) Spatial harmonics of permeance by analytical method.

$$\lambda(x,t) = \lambda_0 + \sum_{m=1}^{\infty}\lambda_m\cos\left[mP_s\frac{2\pi}{L_a}(x - x_0 - v_t t)\right] \tag{3}$$

where

$$\begin{cases} \lambda_0 = \dfrac{P_s}{L_a}(c\lambda_t + d\lambda_s) \\ \lambda_m = \dfrac{2}{m\pi}\left[(\lambda_t - \lambda_s)\sin\left(mcP_s\dfrac{\pi}{L_a}\right)\right] \end{cases} \tag{4}$$

P_s is the effective teeth number of the long stator with P_s = 20, x_0 is the initial position, v_t is the moving speed of the short mover, c and d are the width of the slot and the teeth in the stator, respectively. According to (3), the mP_s (m = 1, 2, 3,...) orders of the permeance harmonics exist, as shown in Fig. 5.

The PM MMF is modulated by the permeance of stator teeth, then, the air-gap normal flux density on no load can be deduced by [16]

$$\begin{aligned} B_{nl}(x,t) &= F(x)\lambda(x,t) \\ &= \lambda_0\sum_{n=1}^{\infty}F_n\cos\left(6n\frac{2\pi}{L_a}x\right) + \sum_{n=1}^{\infty}\sum_{m=1}^{\infty}\frac{1}{2}\lambda_m F_n\left(\cos\beta_1 + \cos\beta_2\right) \\ &\quad + \lambda_0 F_0 + F_0\sum_{m=1}^{\infty}\lambda_m\cos\left[mP_s\frac{2\pi}{L_a}(x - x_0 - v_t t)\right] \end{aligned} \tag{5}$$

where

$$\begin{cases} \beta_1 = (6n + mP_s)\dfrac{2\pi}{L_a}x - mP_s\dfrac{2\pi}{L_a}(x_0 + v_t t) \\ \beta_2 = (6n - mP_s)\dfrac{2\pi}{L_a}x + mP_s\dfrac{2\pi}{L_a}(x_0 + v_t t) \end{cases} \tag{6}$$

Solving (5), the flux density on no load can be predicted with acceptable accuracy, as shown in Fig. 6(a). According to (5), it is also predicted that the $6n$, mP_s, and $|6n \pm mP_s|$ (n, m = 1, 2, 3,…) harmonic orders of the flux density exist, which agrees well with the FE results, as shown in

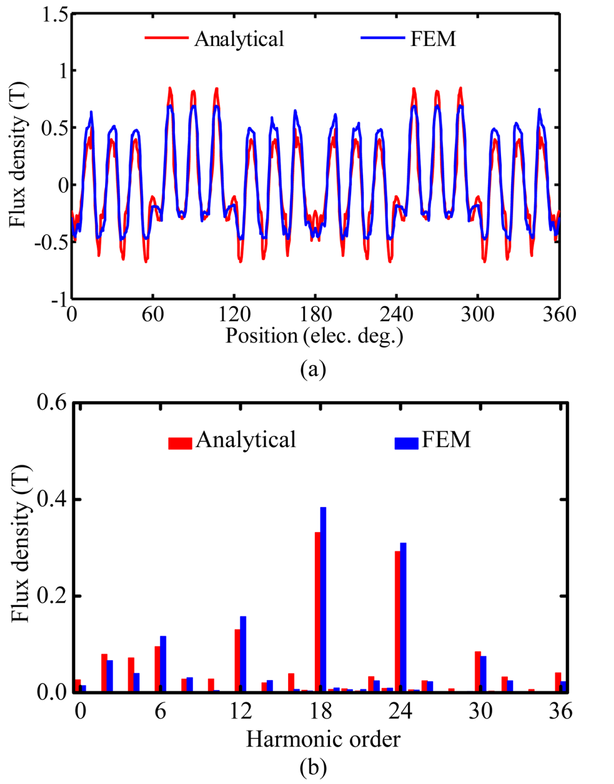

Fig. 6. (Color online) Normal flux density on no load predicted by FE and analytical methods. (a) Waveforms. (b) Harmonics.

Table 1. Spatial harmonics of normal flux density on no load.

Harmonic order	Value	Amplitude
$6n$	6, 12, 18, 24, 30, 36, 42, …	$F_n\lambda_0$
mP_s	20, 40, 60, …	$F_0\lambda_m$
$\lvert 6n\pm mPs\rvert$	2, 4, 8, 10, 14, 16, 22, 26, …	$F_n\lambda_m/2$

Fig. 6(b) and Table 1. It can be seen that some harmonics exist, which result from the modulation of the permeance of stator teeth and the PM MMF. Based on (5) and Figs. 4 and 5, the amplitudes of the mP_s order harmonics $F_0\lambda_m$ are very small, however the amplitudes of the $6n$ order harmonics $F_n\lambda_0$ are relatively high. So, the dominant harmonics of the normal flux density on no load are $6n$, such as the 6th, 12th, 18th, and 24th orders. Moreover, the 2nd flux density harmonic exists. It is primarily caused by the interaction between the 18th PM MMF harmonic and the 20th permeance harmonic of the stator.

3.2. Air-Gap Flux Density on Armature Field

The air-gap windings MMF generated by armature windings is also assumed to be a square wave with an air-gap circumferential position. Both the armature teeth and the split teeth have effects on the MMF, and these effects are separately considered in this study. Fig. 7 shows the air-gap windings MMF with consideration of the armature teeth and the split teeth in the short mover. The phase currents are given as

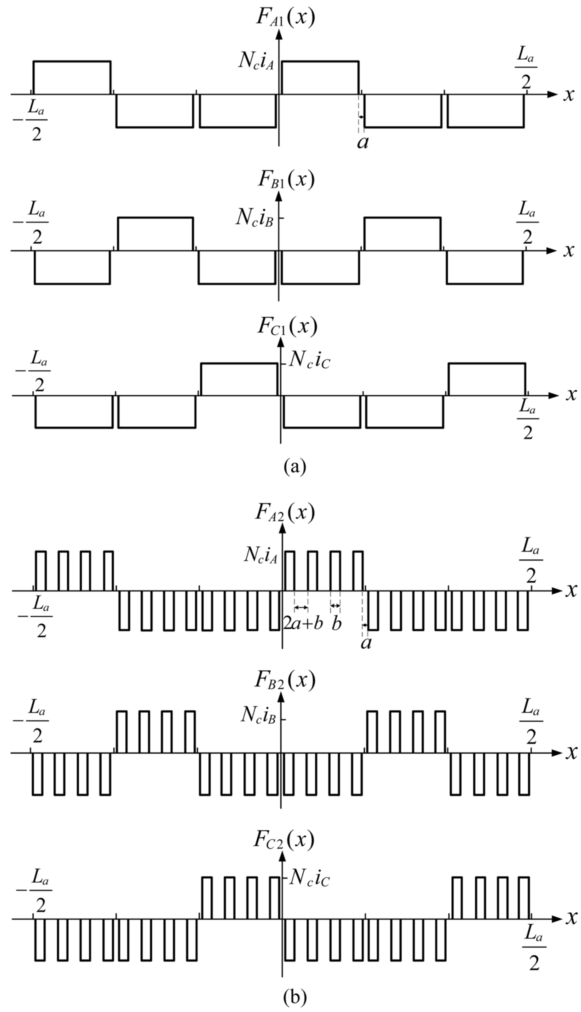

Fig. 7. Armature MMF models. (a) Only considering the armature teeth. (b) Only considering the split teeth.

$$\begin{cases} i_A = I_m \sin(\omega_e t) \\ i_B = I_m \sin(\omega_e t - \dfrac{2\pi}{3}) \\ i_C = I_m \sin(\omega_e t + \dfrac{2\pi}{3}) \end{cases} \tag{7}$$

where I_m is the maximum value of the phase current. The relationship between the electrical angular frequency ω_e and the moving speed of the mover v_t can be expressed as

$$\omega_e = \frac{2\pi}{T_e} = \frac{2\pi v_t}{\tau} \tag{8}$$

where τ is the slot pitch of the stator, T_e is the electrical period.

According to Fig. 7(a), the Fourier series of each phase winding MMF only considering the armature teeth can be derived as

$$\begin{cases} F_{A1}(x,t) = M_{10}i_A + \sum_{n=1}^{\infty} M_{1n}i_A\left[\cos\gamma + 2\sin\left(\frac{n\pi}{3}\right)\sin\gamma\right] \\ F_{B1}(x,t) = M_{10}i_B + \sum_{n=1}^{\infty} M_{1n}i_B\left[2\cos\left(\frac{n\pi}{3}\right) - 1\right]\cos\gamma \\ F_{C1}(x,t) = M_{10}i_C + \sum_{n=1}^{\infty} M_{1n}i_C\left[\cos\gamma - 2\sin\left(\frac{n\pi}{3}\right)\sin\gamma\right] \end{cases} \tag{9}$$

where

$$\begin{cases} M_{10} = -2N_c\left(\frac{1}{6} - \frac{a}{L_a}\right) \\ M_{1n} = -\frac{4N_c}{n\pi}\sin\left(\frac{n\pi}{6} - \frac{n\pi a}{L_a}\right)\cos\left(\frac{n\pi}{2}\right) \end{cases} \tag{10}$$

$$\gamma = \frac{2n\pi}{L_a}x \tag{11}$$

N_c is the number of coil turns of each phase winding.

According to Fig. 7(b), the Fourier series of each phase winding MMF only considering the split teeth can be derived as

$$\begin{cases} F_{A2}(x,t) = M_{20}i_A + \sum_{n=1}^{\infty} M_{2n}i_A\left[\cos\gamma + 2\sin\left(\frac{n\pi}{3}\right)\sin\gamma\right] \\ F_{B2}(x,t) = M_{20}i_B + \sum_{n=1}^{\infty} M_{2n}i_B\left[2\cos\left(\frac{n\pi}{3}\right) - 1\right]\cos\gamma \\ F_{C2}(x,t) = M_{20}i_C + \sum_{n=1}^{\infty} M_{2n}i_C\left[\cos\gamma - 2\sin\left(\frac{n\pi}{3}\right)\sin\gamma\right] \end{cases} \tag{12}$$

where

$$\begin{cases} M_{20} = -\frac{8N_c b}{L_a} \\ M_{2n} = -\frac{16N_c}{n\pi}\sin\left(\frac{n\pi b}{L_a}\right)\cos\left(\frac{2n\pi}{21}\right)\cos\left(\frac{n\pi}{21}\right)\cos\left(\frac{n\pi}{2}\right) \end{cases} \tag{13}$$

Then, the windings MMF considering the armature teeth and the split teeth can be approximatively obtained by

$$F_w(x,t) \approx \frac{1}{2}\sum_{J=A,B,C}\left[F_{J1}(x,t) + F_{J2}(x,t)\right] \tag{14}$$

Based on (10) and (13), when n is even integer (except for the multiples of 3, because the LPMV machine has three phases), that is, n = {2, 4, 8, 10, 14, 16, 20, 22, 26, 28,…}, the MMF of each phase winding exists. When n is odd integer, the M_{1n} and M_{2n} are zero, the MMF of each phase winding does not exist. Then, the windings MMF harmonics of the LPMV machine have {2, 4, 8, 10, 14, 16, 20, 22, 26, 28,…}, that is 6k-2 and 6k-4 orders, where k is a positive integer.

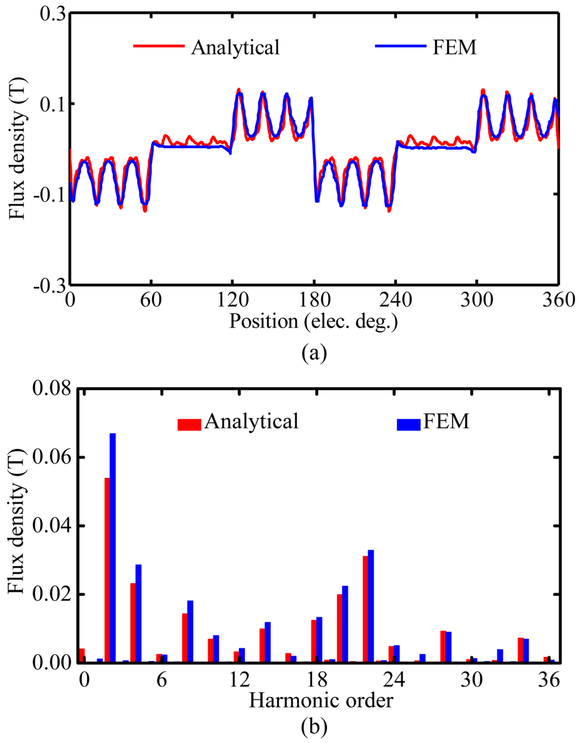

Fig. 8. (Color online) Normal flux density on armature field predicted by FE and analytical methods. (a) Waveforms. (b) Harmonics.

The normal flux density of armature field can be obtained by

$$B_w(x,t) = F_w(x,t)\lambda(x,t) \tag{15}$$

Figure 8 shows the normal flux density of the analytical and FE results. It can be seen that the analytical result agrees well with the FE-predicted one, except that the amplitudes of the FE-predicted harmonics with lower order are slightly higher than the analytical ones. Since the windings MMF $F_w(x, t)$ has 6k-2 and 6k-4 harmonics, and the permeance $l(x, t)$ has mP_s harmonics, the normal flux density of armature field has 6k-2, 6k-4, mP_s, 6k-2 ± mP_s, and 6k-4 ± mP_s harmonics, as shown in Fig. 8(b) and Table 2.

Table 2. Spatial harmonics of normal flux density on armature field.

Harmonic order	Value
6k-2 and 6k-4	2, 4, 8, 10, 14, 16, 20, 22, 26, 28, …
mP_s	20, 40, 60, …
$\lvert 6k-2\pm mP_s\rvert$ and $\lvert 6k-4\pm mP_s\rvert$	0, 2, 4, 6, 8, 10, 12, 14, 16, 18, …

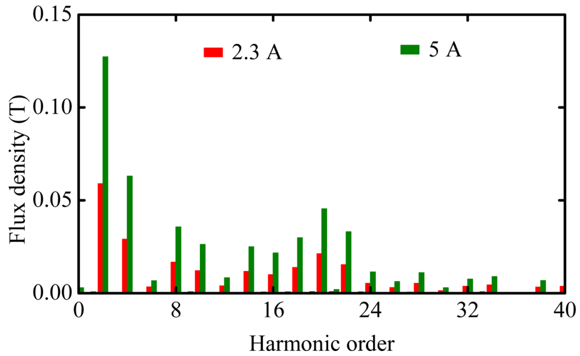

Fig. 9. (Color online) Spatial harmonics of normal flux density on armature field.

Figure 9 shows the spatial harmonics of normal flux density on armature field with different exciting phase currents. It can be seen that each harmonic rapidly increase with the increase of phase current, and the amplitudes of the normal flux density harmonics are proportional to the phase current. Furthermore, the 2nd harmonic which is the dominant component on armature field increases rapidly, and the increment of harmonic amplitude decreases with the increase of the harmonic order.

3.3. Air-Gap Flux Density on Load

The normal flux density on load can be obtained by

$$B_l(x,t) = B_{nl}(x,t) + B_w(x,t) = \left[F(x) + F_w(x,t)\right]\lambda(x,t) \quad (16)$$

Figure 10 shows the spatial harmonics of normal flux density on load and no load. The lower order harmonics instead of the higher order ones rapidly increase with the increase of phase current, because the amplitudes of the normal flux density harmonics on armature field are proportional to the phase current, as shown in Fig. 9. So, with the increase of phase current, the dominant harmonics, such as the 18th and 24th harmonics, are nearly as same as ones on no load, but the lower order harmonics, such as the 2nd and 4th harmonics, are significantly increased, as shown in Fig. 10(b). The rapid variation of the lower order harmonics of flux density on armature field affects the lowest order harmonic of the normal force density, thus seriously affecting the machine vibration, ultimately. Similar to magnetic gears or vernier machines [17, 18], the relationship among the effective pole number of PMs, P_{PM}, the number of active stator teeth, $P_s = 20$, and the pole-pair of armature winding, $P_w = 2$, is given by [10]

$$P_w = \left|P_{PM} - P_s\right| \quad (17)$$

Therefore, the highest-amplitude harmonic order of the normal flux density is modulated to 18, as shown in Fig. 10.

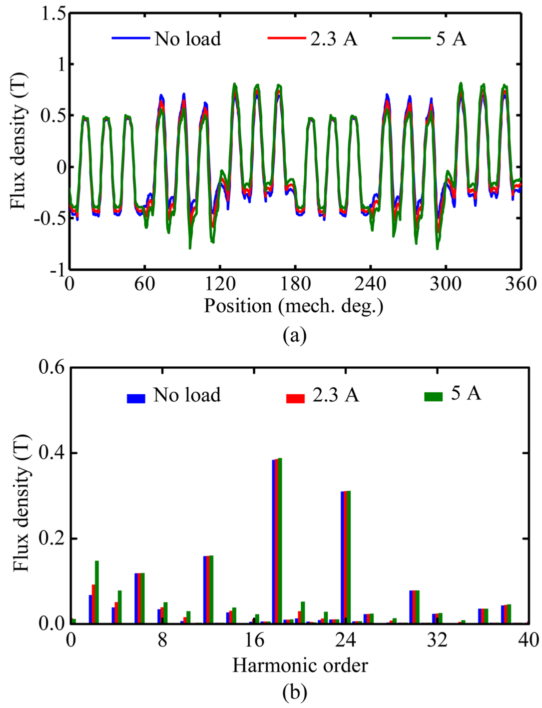

Fig. 10. (Color online) Spatial harmonics of normal flux density. (a) Waveforms. (b) Harmonics.

4. Normal Force and Thrust Force Analyses

4.1. Air-Gap Normal Force Density

By using Maxwell Stress Tensor method which is the popular method to calculate electromagnetic force, the normal force density of the LPMV machine can be calculated from [14]

$$P_y(x,t) = \frac{B_y^2(x,t) - B_x^2(x,t)}{2\mu_0} \approx \frac{B_y^2(x,t)}{2\mu_0} \quad (18)$$

where $B_y(x, t)$ is the y-component flux density, which is the normal flux density, $B_x(x, t)$ is the x-component flux density, and μ_0 is the permeability of air. Generally, the amplitude of x-component flux density is greatly smaller than the normal one, so it can be neglected generally.

Assuming that the harmonic orders of the normal flux density on no load are u_1, u_2, u_3,… and those of the armature field are v_1, v_2, v_3,…, then, according to (18) and the Fourier series of the normal flux density, the orders of the normal force density will be as follows:

1) $q = 2u_i$, $u_i \pm u_j$ $(i = j = 1, 2, 3,\dots)$ which are caused by the PM field only.

2) $q = 2v_i$, $v_i \pm v_j$ $(i = j = 1, 2, 3,\dots)$ which are caused by the armature field only.

3) $q = u_i \pm v_j$ $(i = j = 1, 2, 3,\dots)$ which are caused by the interaction between the PM field and the armature field only.

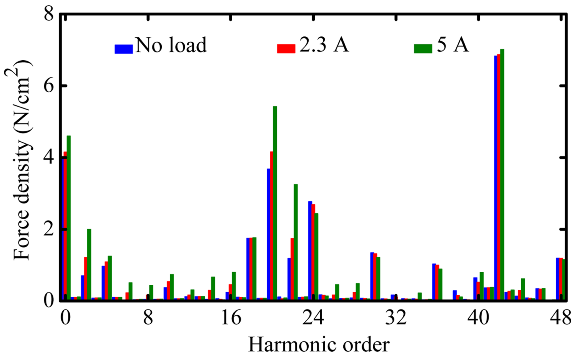

Fig. 11. (Color online) Spatial harmonics of normal force density.

For the LPMV machine, the harmonics of the normal force density on load are richer than that on no load. Fig. 11 shows the spatial harmonics of normal force density in the air-gap under different phase currents. It can be seen that the odd harmonics of normal force density exist due to the margin effect, but the amplitudes are very small and can be neglected. Based on (18), the highest normal force density harmonic is composed of the dominant harmonics of the normal flux density. When the phase current is small or on no load, the highest normal force density component is the 42nd harmonic, which is dominantly composed of the 18th and 24th normal flux density harmonics, as shown in Fig. 12(a). As shown in Fig. 11, the 42nd harmonic changes little with the increase of phase current due to the little change of the 18th and the 24th normal flux density harmonics.

Existing literatures show that the lowest spatial order of the normal force density harmonic results in the lowest vibration mode order, and the lower order normal force harmonics with high-amplitude are very important from the viewpoint of vibration and acoustic noise [19]. Since the vibration of a machine is inversely proportional to the fourth power of the mode order, and proportional to the amplitude of the harmonics. For the LPMV machine, the lowest order of the normal force density harmonics is 2, namely, the greatest common divisor of the effective pole number of PMs P_{PM} and the active stator tooth number P_s, and it will induce high machine vibration and acoustic noise. Furthermore, the radar plots of the normal forces on each split tooth and each PM, as shown in Fig. 13, implies that the dominant vibration mode of the LPMV machine is 2, which is the lowest spatial harmonic order of the normal force density.

The 2nd normal force density harmonic is caused by lots of normal flux density harmonics, such as follows:

1) The interaction between the 20th and 18th harmonics of normal flux density, which is the dominant component.

2) The interaction between the 2nd and 4th harmonics of

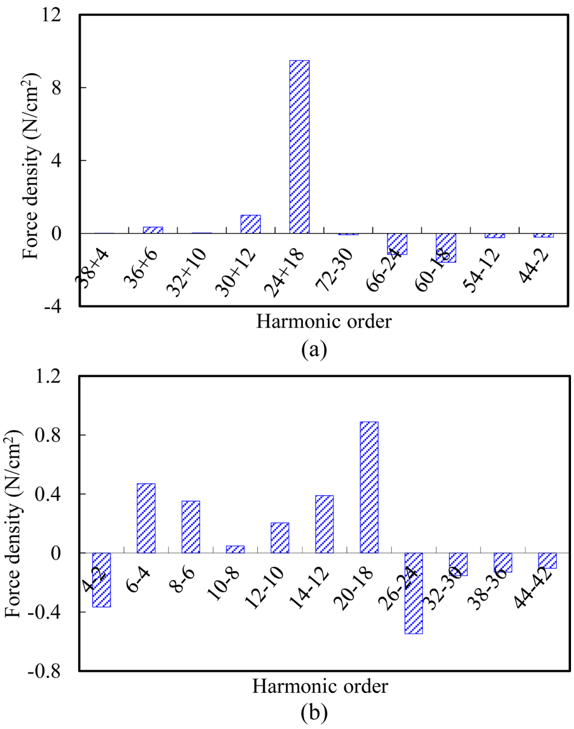

Fig. 12. (Color online) Amplitudes of normal force density harmonic components. (a) 42nd harmonic. (b) 2nd harmonic.

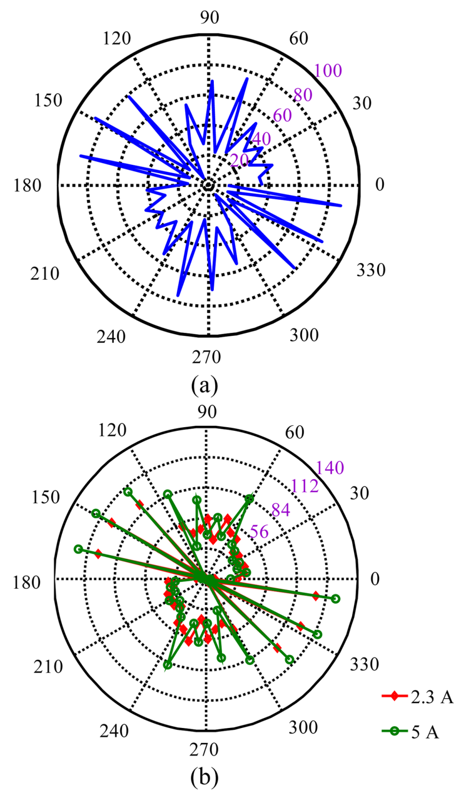

Fig. 13. (Color online) Normal force on each stator tooth and each PM. (a) No load. (b) Load.

normal flux density.

3) The interaction between the 4th and 6th harmonics of normal flux density.

4) The interaction between the 24th and 26th harmonics of normal flux density.

These corresponding amplitudes of radial force density compositions are positive or negative, as shown in Fig. 12(b), and will be offset partly each other. All of these compositions contribute together to the 2nd normal force density harmonic. It can be seen that the amplitude of the 2nd order normal force density harmonic increases obviously with the increase of phase current.

4.2. Normal Force and Thrust Force

The normal force and detent force caused by both the end effect and the slotting effect also exist in the LPMV machine. These force components due to slotting and end effect can be separated. The normal force component of the LPMV machine can be expressed as

$$F_y = F_{y-slot} + F_{y-end} \tag{19}$$

Assuming that the stator length is much larger than the mover length, the stator length is lengthened from 6 to 12 armature teeth, that is, the mover length is two times that of the original one, then, the normal force component is

$$F_{ydouble} = 2F_{y-slot} + F_{y-end} \tag{20}$$

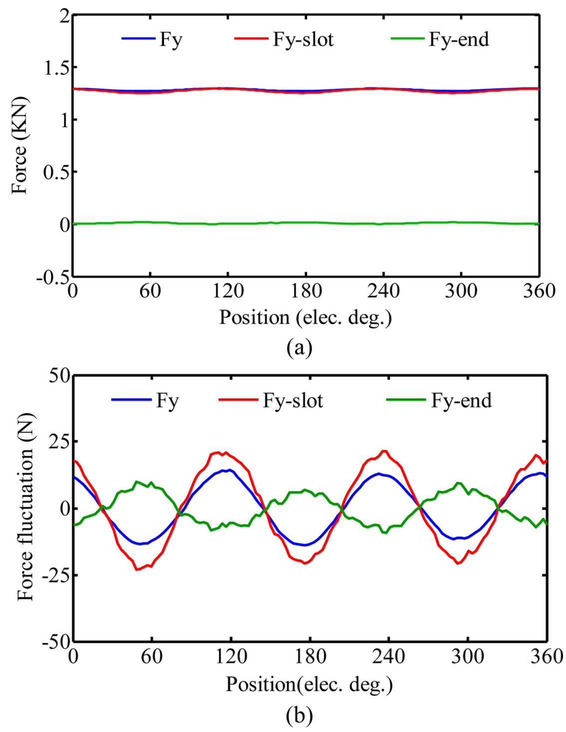

Fig. 14. (Color online) Normal force components due to slotting and end effect. (a) Waveform. (b) Fluctuation.

The normal force component due to slotting effect F_{y_slot} and the component due to end effect F_{y_end} can be obtained by

$$\begin{cases} F_{y-slot} = F_{ydouble} - F_y \\ F_{y-end} = 2F_y - F_{ydouble} \end{cases} \tag{21}$$

Figure 14 shows the separated normal forces and its fluctuations. The fluctuation of F_{y_end} and the one of F_{y_slot} have opposite phase, and partly offset each other, so, smaller normal force fluctuation can be obtained. In addition, as shown in Fig. 14(a), the end effect normal force is much smaller than the slotting effect one and can be neglected.

The forces and force fluctuations under different conditions are shown in Figs. 15 and 16, respectively. It can be seen that the amplitudes of thrust force and normal

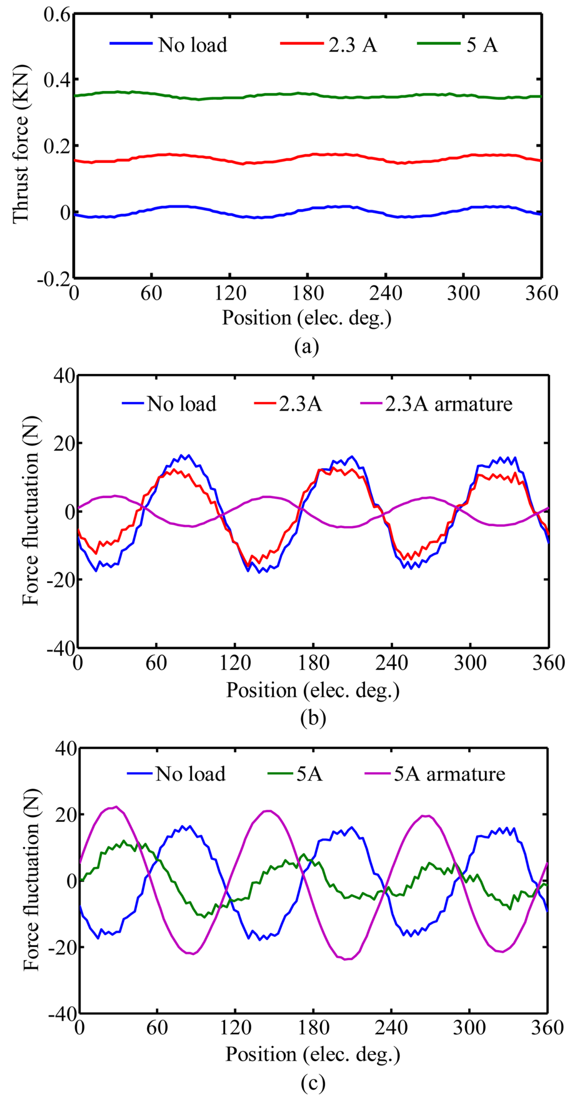

Fig. 15. (Color online) Thrust force. (a) Waveform. (b) Fluctuation at current 2.3 A. (c) Fluctuation at current 5 A.

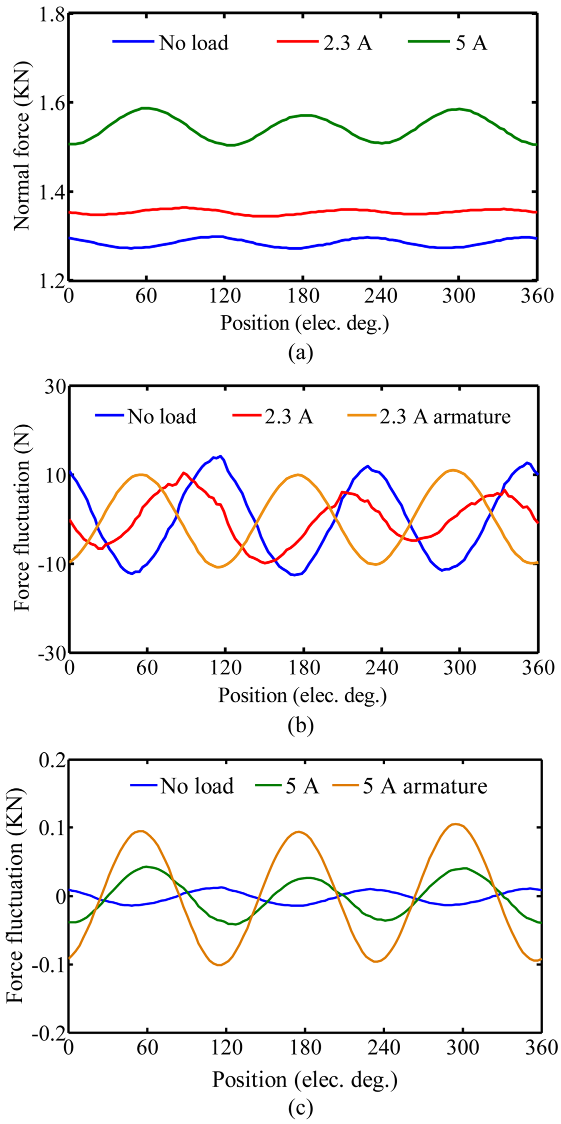

Fig. 16. (Color online) Normal force. (a) Waveform. (b) Fluctuation at current 2.3 A. (c) Fluctuation at current 5 A.

force almost linearly increase with the increase of phase current, as shown in Figs. 15(a) and 16(a). Furthermore, the thrust force fluctuation at current 5 A is the lowest one. Since the thrust force fluctuation on armature field and the cogging force have the difference of 180 electrical degrees, the thrust force fluctuation at current 5 A is lower than the one at current 2.3 A, as shown in Figs. 15(b) and (c). It has been explained in detail by [10]. However, the normal force fluctuation at current 5 A is higher than the others two, as shown in Fig. 16(a). As shown in Figs. 16(b) and (c), the fluctuation on armature field and the one on no load counteract each other. Then, the normal force fluctuation at current 2.3 A is the lowest one. Since the normal force rather than the cogging force plays a more important role for high vibration and noise of the machine [19, 20], so, although the thrust force fluctuation at current 5 A is smaller than the one at current 2.3 A, the vibration at current 5 A will be more severe than the one at current 2.3 A.

5. Vibration Prediction and Verification

The electromagnetic forces acting on the inner surface of the short mover excite the whole mover with corresponding frequency, thus leading to vibration and acoustic noise. The basic dynamic equation for the vibration behavior of a machine can be expressed as

$$[M]\{\ddot{u}\}+[C]\{\dot{u}\}+[K]\{u\}=\{F(t)\} \tag{22}$$

where $[M]$, $[C]$, and $[K]$ are the mass matrix, the damping matrix, and the stiffness matrix of the machine, respectively, $\{F(t)\}$ is the applied equivalent force vectors, $\{u\}$ is the nodal displacement vector.

Modal analysis is a dynamic analysis concerned with natural frequencies and mode shapes of an undamped structure under free vibration. As a result, (22) becomes the eigenvalue problem, and it can be expressed as

$$\left([K]-\omega^2[M]\right)\{u\}=0 \tag{23}$$

The natural mode shapes are calculated through modal analysis by solving (23). The mechanical model is developed by FE method to predict the vibration characteristics of the LPMV machine. As shown in Fig. 17, the natural

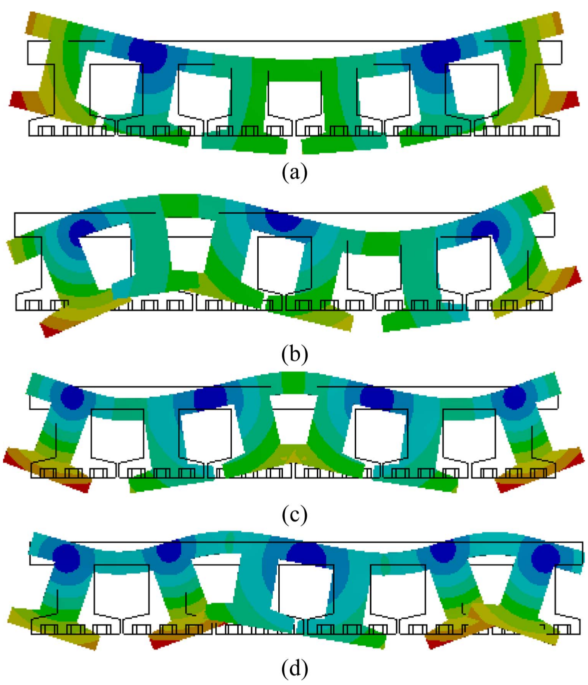

Fig. 17. (Color online) Modal shapes. (a) Mode 1. (b) Mode 2. (c) Mode 3. (d) Mode 4.

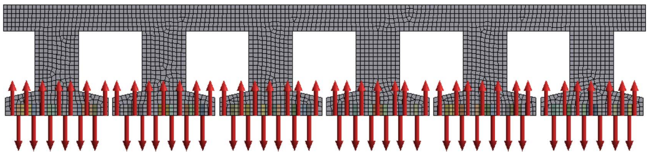

Fig. 18. (Color online) Normal force vectors (red arrows) applied on the mover surface for the initial position.

vibration modes of the short mover are similar to an unrestraint beam, and the yoke mode shapes are sinusoidal waveforms.

Based on the foregoing analysis, the deformation of the short mover is predicted by transient structure analysis. In the transient structural analysis of the mover, only the normal force is applied on the mover surface to investigate the mover vibration, because the tangential force contributes to drag the mover at a constant speed. The tangential force fluctuation contributes to the variation in speed of mover, it is not include in this paper. The normal force density calculated from (18) are transformed to equivalent normal forces acting on the inner surface of the mover by

$$F(t) = \iint_S p_y(x,t)dS \tag{24}$$

where S is the inner surface area of each PM or each split tooth. The equivalent normal force vectors distributed along the inner surface of the mover are shown in Fig. 18.

Figure 19 shows the FE-predicted normal displacement of the short mover. It illustrates that the dominant vibration of the LPMV machine is mode 2, which is just the lowest spatial harmonic order of the normal force density. Moreover, the vibration at current 5 A is obviously more violent than the one at current 2.3 A because of the increase of the 2nd normal force density.

Based on forgoing analysis, since the force fluctuations on the armature and PM fields have a difference of 180 electrical degrees, the thrust and normal force fluctuations at different phase currents are different, thus resulting in different extent vibration. Figures 20 and 21 show the FE-predicted normal acceleration and the harmonics of the short mover, respectively. It can be seen that the frequency of the first peak is about 584 Hz, and the second peak occurs at the 2629 Hz. The first acceleration peak is the dominant vibration component. In order to verify the theoretical analysis, the modal frequencies and the normal accelerations under different conditions are measured by an IEPE acceleration sensor, as shown in Fig. 22. It can be seen that the first and second modes are stimulated by modal hammering method, and the dominant vibration

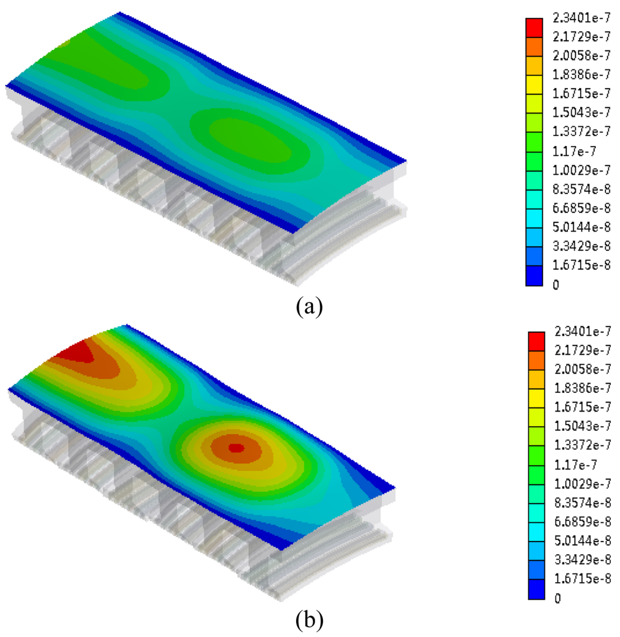

Fig. 19. (Color online) Normal displacement on the mover face. (a) At current 2.3 A. (b) At current 5 A.

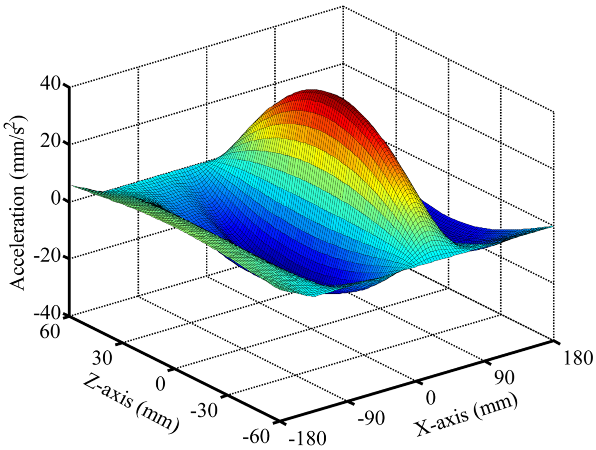

Fig. 20. (Color online) FE-predicted normal acceleration on the mover face.

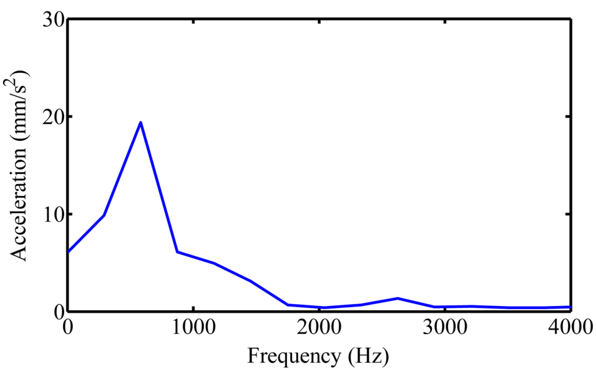

Fig. 21. (Color online) FE-predicted normal acceleration harmonics.

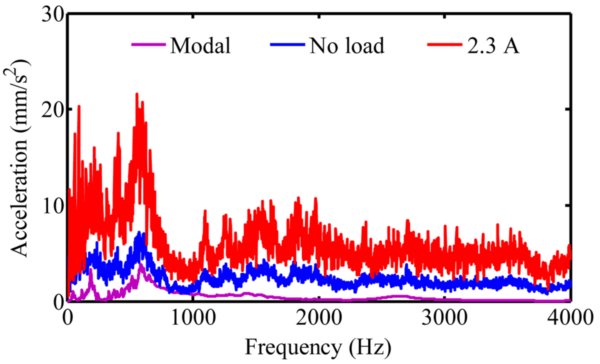

Fig. 22. (Color online) Measured normal acceleration and modal frequency.

occurs at the second order frequency, that is 584 Hz. The first mode with frequency 188 Hz maybe stimulated by the experimental platform or some unbalance factors, such as the magnetic grating ruler or other mechanical assembly. The acceleration amplitude at current 2.3 A is larger than the one on no load. It is because that the lower order harmonic of normal force density at current 2.3 A is larger than the one on no load, although the normal force fluctuation is smaller. It also illustrates that the lower-order normal force density harmonic with high-amplitude is the dominant vibration source of the LPMV machine. Good agreement can be seen among the magnetic force analysis, the predicted vibration order, and the measured results. It should be mentioned that the operation at rated phase current 5 A is very difficult because of the experimental platform. So, this paper only gives the experimental results operated at 2.3 A and no load to verify the theoretical analysis.

6. Conclusion

This paper has investigated the normal force and vibration characteristics of the three-phase LPMV machine. The flux density has been analyzed by the MMF and the air-gap surface permeance, and the normal force density has been calculated by Maxwell Stress Tensor method. Then, the main vibration modes and the vibration behavior of the mover have been determined by structural analysis. Finally, the experimental results have been given for verification. It can be confirmed that the dominant vibration mode can be determined from the lowest harmonic of the normal force density, and the reduction of the lowest-order normal force density harmonic can mitigate the machine vibration. This conclusion is similar to the one of the rotation PM machines, and it is instructive for the design of a high-precision and low-vibration LPMV machine.

Acknowledgment

This work was supported by the National Natural Science Foundation of China (51577084 and 51407086), by the Research Fund for 333 Project of Jiangsu Province (BRA2015302), by the Key Project of Natural Science Foundation of Jiangsu Higher Education Institutions (15KJA470002), by the Priority Academic Program Development of Jiangsu Higher Education Institutions, and by the Research Foundation for Advanced Talents of Jiangsu University (1283000203).

References

[1] W. Zhao, M. Cheng, K. T Chau, R. Cao, and J. Ji, IEEE Trans. Ind. Electron. **60**, 151 (2013).
[2] R. Cao, M. Cheng, and B. Zhang, IEEE Trans. Ind. Electron. **62**, 4056 (2015).
[3] K. H. Shin, K. H. Jeong, J. Y. Choi, K. Hong, and K. H. Kim, J. Magn. **20**, 432 (2015).
[4] J. Chang, J. Kim, D. Kang, and D. Bang, J. Magn. **15**, 64 (2010).
[5] N. Hodgins, O. Keysan, A. S. McDonald, and M. A. Mueller, IEEE Trans. Ind. Electron. **59**, 2094 (2012).
[6] P. Jin, Y. Yuan, H. Lin, S. Fang, and S. L. Ho, J. Magn. **18**, 95 (2013).
[7] T. W. Ching, K. T. Chau, and W. Li, IEEE Trans. Magn. **52**, 8204804 (2016).
[8] Y. Du, M. Cheng, K. T. Chau, X. Liu, F. Xiao, and W. Zhao, IET Electr. Power Appl. **9**, 203 (2015).
[9] Z. Liu, W. Zhao, J. Ji, and Q. Chen, IEEE Trans. Magn. **51**, 8105807 (2015).
[10] J. Ji, W. Zhao, Z. Fang, J. Zhao, and J. Zhu, IEEE Trans. Magn. **51**, 8106710 (2015).
[11] W. Zhao, J. Zheng, J. Wang, G. Liu, J. Zhao, and Z. Fang, IEEE Trans. Ind. Electron. **63**, 2072 (2016).
[12] W. Li, K. T. Chau, C. Liu, S. Gao, and D. Wu, IEEE Trans. Magn. **49**, 3949 (2013).
[13] A. L. Shuraiji, Z. Q. Zhu, and Q. F. Lu, IEEE Trans. Magn. **52**, 9500406 (2016).
[14] S. A. Kim, Y. W. Zhu, S. G. Lee, S. Saha, and Y. H. Cho, IEEE Trans. Magn. **50**, 4001204 (2014).
[15] T. K. Hoang, D. H. Kang, and J. Y. Lee, IEEE Trans. Magn. **46**, 3795 (2010).
[16] Z. Z. Wu and Z. Q. Zhu, IEEE Trans. Magn. **51**, 8105012 (2015).
[17] C. Liu, K. T. Chau, and Z. Zhang, IEEE Trans. Magn. **49**, 4180 (2012).
[18] D. K. Jang and J. H. Chang, IEEE Trans. Magn. **50**, 7021704 (2014).
[19] Z. Q. Zhu, Z. P. Xia, L. J. Wu, and G. W. Jewell, IEEE Trans. Ind. Appl. **46**, 1908 (2010).
[20] M. S. Islam, R. Islam, and T. Sebastian, IEEE Trans. Ind. Appl. **50**, 3214 (2014).